The Journal of Chemical Physics

Asymmetric and long range interactions in shaken granular media

Cite as: J. Chem. Phys. **151**, 164903 (2019); https://doi.org/10.1063/1.5123304
Submitted: 04 August 2019 . Accepted: 14 October 2019 . Published Online: 30 October 2019

Joan Codina, and Ignacio Pagonabarraga

The Journal of Chemical Physics ARTICLE scitation.org/journal/jcp

Asymmetric and long range interactions in shaken granular media

Cite as: J. Chem. Phys. 151, 164903 (2019); doi: 10.1063/1.5123304
Submitted: 4 August 2019 • Accepted: 14 October 2019 •
Published Online: 30 October 2019

Joan Codina[1,2,3] and Ignacio Pagonabarraga[3,4,5,a)]

AFFILIATIONS

[1]Wenzhou Institute, University of Chinese Academy of Sciences, 325001 Wenzhou, China
[2]Institute of Physics, Chinese Academy of Sciences, 100190 Beijing, China
[3]Departament de Física de la Matèria Condensada, Universitat de Barcelona, C. Martí i Franquès 1, Barcelona 08028, Spain
[4]Universitat de Barcelona Institute of Complex Systems (UBICS), Universitat de Barcelona, 08028 Barcelona, Spain
[5]CECAM Centre Européen de Calcul Atomique et Moléculaire, École Polytechnique Fédérale de Lausanne, Batochimie, Avenue Forel 2, 1015 Lausanne, Switzerland

[a)]**Electronic mail:** ipagonabarraga@ub.edu

ABSTRACT

We use a computational model to investigate the emergence of interaction forces between pairs of intruders in a horizontally vibrated granular fluid. The time evolution of a pair of particles shows a maximum of the likelihood to find the pair at contact in the direction of shaking. This relative interaction is further studied by fixing the intruders in the simulation box where we identify effective mechanical forces and torques between particles and quantify an emergent long range attractive force as a function of the shaking relative angle, the amplitude, and the packing density of grains. We determine the local density and kinetic energy profiles of granular particles along the axis of the dimer to find no gradients in the density fields and additive gradients in the kinetic energies.

I. INTRODUCTION

Granular matter has attracted recent attention because of its intrinsically different nature as compared to equilibrium solid, liquid, and gas states;[1] due to its ubiquity in industry in the form of plastic beads, sand, as well as edible grains, i.e., coffee and wheat; and because of jamming and clogging processes and stress distribution which lead to the formation of stable structures. Jamming in granular matter has been widely studied in the past.[2,3]

Shaken granular matter is an actuated system out of equilibrium due to a steady flux of energy from the container to the grains that is finally dissipated through contact interactions. Striking phenomena occur in mixtures of particles where shaking leads to species segregation ranging from clusters to stripes.[4–6] The best known manifestation of this granular separation is the so-called Brazil nut effect.[7–9] For horizontally driven matter, gravity is no longer a relevant parameter, and a mixture can phase separate into stripes orthogonal to the shaking direction[10–13] or even form clusters for swirling shakings.[14] Understanding the ability of granular mixtures to demix is of direct industrial relevance and can help explain diverse phenomena, such as stratification in terrestrial environments or in asteroid or planetoid formation.[15]

As a paradigmatic example of the qualitative change that granular systems experience under shaking, we have the case of granular flow through a bottleneck—like the flow of sand in an hourglass. Under the sole effect of a constant force, such as gravity, the granular flow can be spontaneously interrupted[16,17] if the exit is not wide enough. On the contrary, for granular matter under shaking, the nature of the flux interruption dramatically changes and the system, once clogged, may spontaneously unclog.[18]

In the nonequilibrium state induced by shaking, granular matter has been reported to fluidize for vertical and horizontal[19–21] forcing. Once granular matter fluidizes, large density fluctuations have been reported and such a situation leads to the opening of Casimir-like scenarios[22] for the effective granular interactions.[23]

Band segregation for a binary mixture of horizontally agitated granular matter has been analyzed in terms of attractive and anisotropic pairwise interactions between inclusions.[24] However, the details of the interactions were not directly addressed. Position tracking experiments of metallic spheres immersed in a dense poppy-seed granular monolayer have revealed not only an attraction between a pair but an aligning interaction relative to the shaking direction.[25] Following this experimental evidence, we present this model that captures and quantifies the pair interaction between intrusive particles.

This paper is structured as follows. In Sec. II, we present a model for both grains and inclusions under horizontal vibration. In Sec. III, we study the free motion of an intruder pair in a shaken granular bed and identify the probability to locate particles as a function of their separation. In Sec. IV, we fix the inclusion pair in order to quantify the emergent effective radial and tangential forces; the mechanical formation energy of the dimers is then compared to the pair distance distribution previously obtained in Sec. IV; and finally, the effect of the pair in the kinetic energy of the granular bed is explained.

II. MODEL

Recent experiments have studied the dynamics and structure of a pair of phosphor-bronze spheres immersed in a horizontally shaken monolayer of poppy seeds. Poppy seeds are kidney shaped granular particles with typical diameters ranging 0.5 mm–1 mm with a material density of $\rho = 0.2$ g cm^{-3}. Poppy seeds have a wide contact area with the surface of the tray, so their friction is large, and periodically displace with the vibrated tray. Bronze spheres, on the contrary, are smooth and uniform in size with a diameter of 1.5 mm and a material density[26] of $\rho = 8.8$ g cm^{-3}.

Spheres easily rotate on the vibrated flat surface of the system,[26] whereas grains have a tendency to follow the moving tray. Inspired by this situation, and as sketched in Fig. 1, we consider a simplified two dimensional model for the dynamics of grains and inclusions which captures the essential features of the forced grain monolayer and develop an integration scheme to computationally solve the equations of motion of the granular system.

A. Equations of motion

We treat grains as N disks at positions $\boldsymbol{x}$ of diameter σ, drawn from a uniform distribution with average $\langle\sigma\rangle = \sigma_g$ and 10% dispersion to account for experimental polydispersity,[25] in a 2d periodic box of side L. We define an averaged packing fraction of the monolayer as $\phi = N\pi\langle\sigma^2\rangle/(4L^2)$. Each grain with a mass that depends on their diameter as $m_i = m_0(\sigma_i/\sigma_g)^3$, where m_0 is the mass of a grain of size σ_g. Grains are periodically driven with the tray velocity $\boldsymbol{v}_s(t)$. Bronze spheres, inclusions, are modeled as disks of diameter $\sigma = 1.5\sigma_g$ and mass $M = 50\, m_0$ at positions $\boldsymbol{X}$. Experimental observations indicate that inclusions roll on the vibrating plate, and hence, we can consider inclusions not being displaced by the plate. We then consider the dynamics of the inclusions not to be altered by the substrate velocity $\boldsymbol{v}_s$. At larger packing densities of the granular bed, inclusions will be unable to rotate solidly with the substrate due to the interactions with the grains. Therefore, we incorporate a dissipative term in the dynamics of the inclusions $-\gamma_s d\boldsymbol{X}/dt$ that accounts for the sliding of inclusions on the substrate. In an effective way, the friction term associated with the dynamics of the inclusion accounts for the hindrance of the rotation.

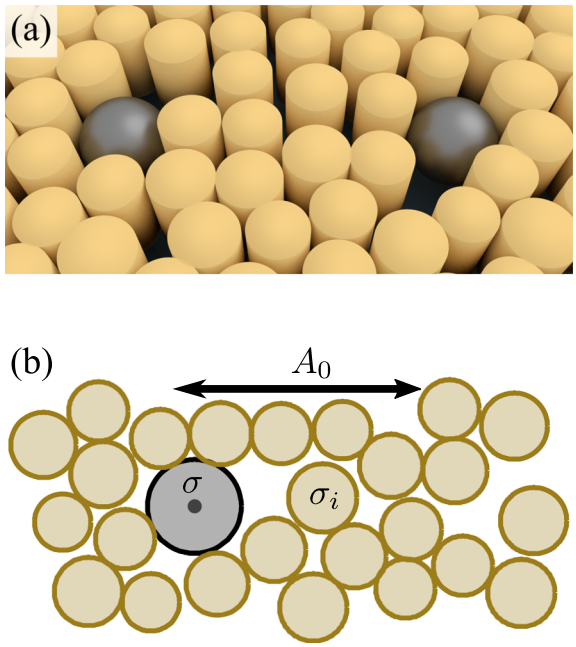

FIG. 1. Representation of the granular system. (a) Granular particles have a large contact area with the shaking surface and are modeled as cylinders, whereas rotating inclusions are modeled as spheres. (b) Projection of the shaken granular system in the shaking plane.

For each particle, either grain, $\boldsymbol{x}_i$, or inclusion, $\boldsymbol{X}_i$, we present its corresponding equation of motion,

$$m_i \frac{d^2\boldsymbol{x}_i}{dt^2} = -\gamma_{s,i}\left(\frac{d\boldsymbol{x}_i}{dt} - \boldsymbol{v}_s(t)\right) + \boldsymbol{F}_i^c + \boldsymbol{F}_i^d + \boldsymbol{F}_i^r\,, \tag{1}$$

$$M \frac{d^2\boldsymbol{X}_i}{dt^2} = -\gamma_{s,i}\frac{d\boldsymbol{X}_i}{dt} + \boldsymbol{F}_i^c + \boldsymbol{F}_i^d + \boldsymbol{F}_i^r\,, \tag{2}$$

where we introduce an oscillatory velocity of the tray, $\boldsymbol{v}_s(t) = A_0\omega \sin\omega t\hat{\boldsymbol{e}}_x$, characterized by its displacement amplitude, A_0, and frequency, ω. The motion of the grains relative to the tray introduces a friction force whose magnitude $\gamma_{s,i}(d\boldsymbol{x}_i/dt - \boldsymbol{v}_s)$ depends on the velocity of the grain relative to the tray and a dissipation constant, $\gamma_{s,i}$, proportional to the contact area of the disk, σ_i^2.

The excluded volume interaction among particles, as well as the energy dissipated in particle collisions, is described through a linear spring-dashpot model for the interactions between particles. The total conservative and dissipative forces on particle i are pairwise additive, $\boldsymbol{F}_i^{(c/d)} = \sum_j \boldsymbol{F}_{ij}^{(c/d)}$, that activate when grains overlap.[20,27,28] The degree of compression between two disks i and j is quantified by $\xi_{ij=(\sigma_j+\sigma_i)/2-|\boldsymbol{r}_j-\boldsymbol{r}_i|}$. Accordingly, the elastic pairwise conservative force reads

$$\boldsymbol{F}_{ij}^c = -k\xi_{ij}\theta(\xi_{ij})\hat{\boldsymbol{n}}_{ij}\,, \tag{3}$$

with k as an elastic constant (a material dependent parameter) and $\hat{\boldsymbol{n}}_{ij} = (\boldsymbol{r}_j - \boldsymbol{r}_i)/(|\boldsymbol{r}_j - \boldsymbol{r}_i|)$ as the center-center unit vector. $\boldsymbol{F}^c_{ij}$ does not vanish only when the two disks overlap, i.e., $\xi_{ij} > 0$ as accounted to by the Heaviside function, $\theta(\xi)$.

The dissipative pairwise interaction, responsible of the energy loss, reads

$$\boldsymbol{F}^d_{ij} = \gamma_n(\boldsymbol{v}_{ij}\cdot\boldsymbol{n}_{ij})\theta(\xi_{ij})\boldsymbol{n}_{ij}\,, \tag{4}$$

with γ_n as a dissipation constant, $\boldsymbol{v}_{ij} = \boldsymbol{v}_j - \boldsymbol{v}_i$, and its direction opposes the direction of the relative velocity between pairs. This dissipation mechanism between pairs may lead to configurations of small overlaps with the elastic and dissipative forces canceling each other. In these situations, pairs of particles tend to remain close to each other. To avoid such computational artifacts, as proposed in Ref. 28, we use the total force of interaction between pairs to be always either repulsive or zero, $\boldsymbol{F}_{ij} = \max(0, (\boldsymbol{F}^c_{ij} + \boldsymbol{F}^d_{ij})\cdot\hat{\boldsymbol{n}}_{ij})\,\hat{\boldsymbol{n}}_{ij}$.

Additionally, we introduce random forces, $\boldsymbol{F}^r$, to account for irregularities and vertical collisions. The source of noise is Gaussian for each component with zero mean and variance, $\langle \hat{\boldsymbol{e}}_\alpha\cdot\boldsymbol{F}^r_i(t)\hat{\boldsymbol{e}}_\beta\cdot\boldsymbol{F}^r_j(t')\rangle = 2\Lambda_\alpha\delta_{ij}\delta_{\alpha\beta}\delta(t-t')$. The Λ_α parameter accounts for the asymmetry in the noise strength in the parallel and perpendicular directions relative to the tray shaking.

In Secs. III and IV, we will consider the tray oscillation period $\tau^{-1} = 2\pi\omega$, the average grain size σ_g, and its mass m_0 as time, length, and mass units, respectively. In terms of these magnitudes, we define the elastic constant k and the dissipation constants γ_n, and γ_s, and Λ_x with standard values present in the literature[19] and given in Appendix B. The integration of the equations is performed by a stochastic integrator inspired by Ref. 29 and detailed in Appendix A.

In Appendix B, we characterize a bed of granular particles and analyze their kinetic energies. We observe that the packing fraction of the grain monolayer has an impact on the inclusion energy loss above $\phi = 0.6$, whereas beyond $\phi \approx 0.75$ the dynamics of the grains slows down, and the displacement statistics of grains show the caging effects introduced by the formation of a quasicrystalline structure of the grains. In the rest of this paper, we consider granular beds within the density range $\phi \in [0.6, 0.75]$.

III. FREE MOVING DIMER

In order to analyze the emergent features induced by a forced granular system on embedded intruders, we will analyze the dynamics of a pair of intruders. To this end, we consider the free evolution of a dimer of inclusion particles in a granular bed. In Sec. III A, we define the relative coordinates that describe the pair motion. In Sec. III B, we extract the relative arrangement of the inclusion pair from its evolution as a function of the granular shaking amplitudes and packing fractions. Finally, in Sec. III C, we analyze the averaged probability distribution of the pair relative positions to measure the pair separated by a distance d and the relative orientation for both touching and distant pairs.

A. An inclusion dimer

In a periodically driven granular system, the energy is introduced by the external forcing through both A_0 and ω. On the one hand, the shaking amplitude A_0 introduces a length scale that may lead to structural system deformations of typical length $\sim 2A_0$. On the other hand, the shaking frequency ω modifies the dissipation rate of the granular system. In this paper, we control the tray vibration by changing the shaking amplitude, A_0, and fixing its frequency.

A doublet of intruders of diameter σ, $\{\boldsymbol{X}_a, \boldsymbol{X}_b\}$, defines a dimer whose center-center vector is $\boldsymbol{r} = \boldsymbol{X}_a - \boldsymbol{X}_b$. The position vector $\boldsymbol{r} = (r_x, r_y)$ is equally described by its modulus r and angle α relative to the shaking direction, $\boldsymbol{r} = r(\cos\alpha,\ \sin\alpha)$. We define a "parallel" ("perpendicular") configuration of the dimer for a configuration $\alpha \approx 0$ $(\pi/2)$. For simplicity, we also use the distance between the surfaces of inclusions $d = r - \sigma$ to define the dimer separation.

B. Probability landscapes

In order to understand the dynamics of a dimer of intruders in a shaken granular bed, we have prepared a large collection of initial conditions with $d \in [4, 7]$ and $\alpha \in [0, 2\pi]$ to sample between 10^6 ($\phi = 0.6$) and $6\cdot 10^6$ ($\phi = 0.75$) cycles for systems of box size $L = 32\sigma_g$ at shaking amplitudes $A_0 = 0.75\sigma_g$ and $A_0 = 1.5\sigma_g$.

We define $\mathcal{P}(r_x,\ r_y)$ as the probability to measure the dimer in a configuration with $r_x \in [r_x, r_x + \Delta x]$ and $r_y \in [r_y,\ r_y + \Delta y]$, where $\Delta x = \Delta y = 0.05\sigma_g$, which results from simulations sampling at each shaking cycle. From this probability, we can extract $-\ln\mathcal{P}(r_x, r_y)$, which identifies the most probable configurations of the dimer freely evolving in the granular bed. If the system were in equilibrium, the logarithm of the probability $-\ln\mathcal{P}$ would be proportional to the energy landscape $\mathcal{U}(r_x, r_y)$ of the system. We leave the comparison between $\mathcal{P}$ and the dimer mechanical formation energy, U, for Sec. IV C. Here, we associate minima of the magnitude $-\ln P$ to more probable configurations (effective attractions) and maxima to more unlikely configurations (effective repulsions). Probability landscapes $-\ln\mathcal{P}(r_x, r_y)$, see Fig. 2, identify $r \approx \sigma$ as the most probable pair distance for all studied granular beds. Additionally, all four granular beds show a high degree of anisotropy at contact, $r \approx \sigma$, where $-\ln\mathcal{P}(\sigma, \alpha)$ is always smaller for $\alpha \approx 0$ than for $\alpha \approx \pi/2$. This clear asymmetry shows a strong tendency of dimer to align in the shaking direction.

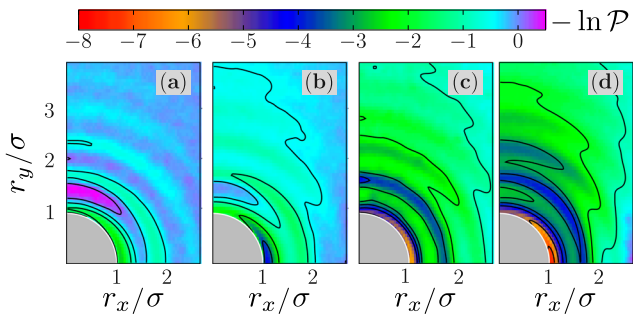

FIG. 2. Landscape of dimer configurations. The heat map with solid contour lines of $-\ln\mathcal{P}$ as a function of the relative configuration of the dimer, (r_x, r_y), for different grain packing fractions, ϕ, and forcing strength, A_0. The gray shaded regions correspond to configurations of $(r_x/\sigma)^2 + (r_y/\sigma)^2 < 1$ and thus cannot be reached by the inclusion. The x-component is aligned with the sinusoidal forcing imposed on the tray. From left to right: (a) $A_0 = 0.75\sigma$ and (b) $A_0 = 1.5\sigma$ for $\phi = 0.6$; (c) $A_0 = 0.75\sigma_g$ and (d) $A_0 = 1.5\sigma_g$ for $\phi = 0.75$.

The structure of the granular bed is clearly manifested in the probability landscape as a sequence of concentric oscillating rings. At long distances from contact, contour lines manifest the anisotropy of the interaction. Moreover, the probability landscape decays faster along the shaking direction than perpendicular to it.

Figure 3 further details the probability landscape for $A_0 = 1.5\sigma_g$ and packing fraction $\phi = 0.75$. The granular structure is rapidly lost in the parallel direction, whereas it shows stronger persistence for configurations where the dimer is oriented perpendicular to the tray shaking direction. At long distances, we observe that perpendicular configurations are favored and an island of repulsion emerges centered at $r = 8\sigma_g$ and $\alpha = 0$.

C. Marginal probability densities

We can provide a more compact description of the distance and angular dependence that characterize the dimer interaction through the corresponding marginal probability densities. These quantities are also more attractive experimentally because they require less statistics. Specifically, we quantify the distance behavior of $\mathcal{P}$ through $P(r)$, the averaged angular distribution, obtained by integrating $\mathcal{P}(r, \alpha)$ over the angular configurations of the dimer.

Figure 4 displays the angular averaged probability density, $P(d)$, as a function of $d = r - \sigma$, so that $d = 0$ corresponds to the contact position $r = \sigma$. We identify three different features in $P(d)$. First, at contact ($d = 0$), $-\ln P(d)$ reaches its lowest value; hence, it is the preferred and most probable configuration. Second, the oscillations of $-\ln P(d)$ at short distances clearly show the structure of the bed since the periodicity corresponds to the granular size. The surroundings of minima are locally stable and correspond to an integer number of grains in the internal region of the inclusion dimer. Third, the oscillations are superimposed on a monotonous decay toward zero. The stronger the decay is, the more compact the system is—the signal is stronger at $\phi = 0.75$. Within the available range of distances, we have tested that the decay in $-\ln P(d)$ is compatible with an algebraic tail $-\ln\left(P(d)/P(\infty)\right) \sim d^{-1}$, shown as dashed lines in Fig. 4.

To quantify anisotropy, we compute the conditional probability densities $P_<(r^\star; \alpha)$ and $P_>(r^\star; \alpha)$ as integrals of $\mathcal{P}(r, \alpha)$ over r in the ranges $r \in (\sigma, \sigma + r^\star)$ and $r \in (\sigma + r^\star, \infty)$ for $P_<$ and $P_>$, respectively. $P_{<(>)}(r^\star; \alpha)$ quantifies the anisotropy of the configurations of the dimer at short(long) distances.

The angular distributions displayed in Fig. 5 have been obtained for $r^\star = 2\sigma_g$. At short distances, $P_<(2\sigma; \alpha)$, we observe a preference for parallel configurations. The anisotropy in the configurations has a major dependence on the shaking amplitude, while it shows a mild dependence on packing density. At larger distances, $d > 2\sigma_g$, on the contrary, the dimer tends to orient perpendicular to the shaking direction. In this case, the degree of anisotropy is relatively weak except for large densities and shaking amplitudes, $\phi = 0.75$ and $A_0 = 1.5\sigma$, where the anisotropy increases revealing the instability island clearly appreciable in the 2d heat map in Fig. 3.

If the system were to be in equilibrium, the interpretation of the probabilities would be straightforward. The minimum and

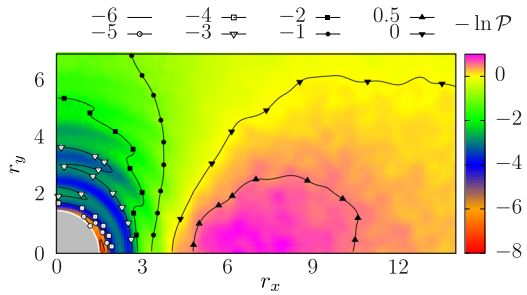

FIG. 3. Anisotropy in the dimer configurations. The heat map with solid contour lines of the landscape, $-\ln \mathcal{P}$, for a system at $\phi = 0.75$ and $A_0 = 1.5\sigma_g$, an extension in the r domain of Fig. 2 to show the long distance behavior. To fully comprehend the behavior of $-\ln \mathcal{P}$, we introduce different symbols in the contour lines, as detailed in the upper key. We observe an exclusion zone, in magenta, where the probability to find the dimer is below the value of $\mathcal{P}$ at infinity.

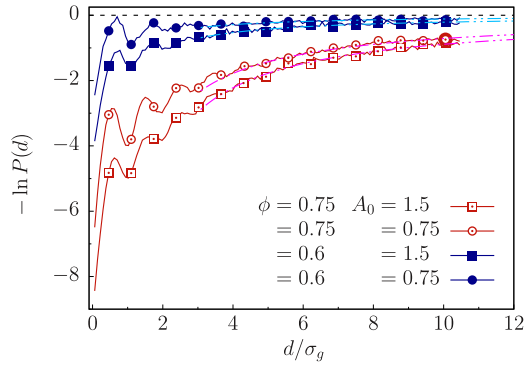

FIG. 4. Angular averaged probability density. The plot for different values of the packing density ϕ and shaking amplitude A_0. As a guide to the eye, we plot the fitted $-\ln P(d) = a/d$ in cyan and magenta.

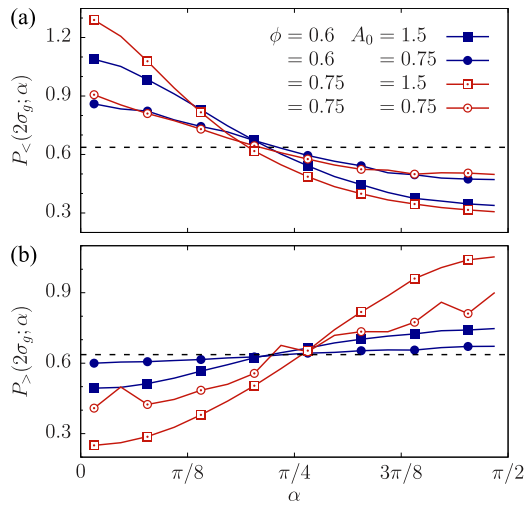

FIG. 5. Angular dependence of the conditional probability densities as a function of ϕ and A_0. (a) For distances $d < 2\sigma_g$. (b) For distances $d > 2\sigma_g$. Black dashed lines display the value of an isotropic distribution, $2/\pi$.

slow decay of the radial probability $-\ln P(d)$ would translate into an energy minimum at $d = 0$ and an emergent attractive long range interaction $U \sim d^{-1}$. The results in the anisotropy shown in Fig. 5(a) would imply the emergence of an aligning torque at short distances, a torque that would align the dimer toward the shaking direction. However, the system is not in equilibrium, and thus, we cannot relate the probability of the dimer configurations to the interaction energies in the system. In Sec. IV, we compute mechanically the effective interaction forces and formation energies of a dimer following similar procedures to the ones used by Refs. 30–32.

IV. FIXED INCLUSIONS

In this section, we mechanically compute the effective interaction forces and formation energies for an inclusion dimer. As seen in Figs. 2–4, the free evolution of the dimer strongly favors configurations at short inclusion-inclusion separation distances. The measure of the relative forces, $\boldsymbol{F}_2(\boldsymbol{R}_2) - \boldsymbol{F}_1(\boldsymbol{R}_1)$, following the dynamics concentrates on the sampling of the interaction at short separation distances, whereas long distance configurations are explored less efficiently. In equilibrium systems, methods such as umbrella sampling[33–35] have given astonishing results in the exploration of nontrivial energy landscapes where an external bias permits the system to explore states that are otherwise computationally expensive to explore. The out of equilibrium nature of the considered system does not provide a systematic method to extract such an external bias. To overcome this difficulty, we prepare systems with fixed values of the dimer configuration (r, α) and freeze its evolution during the granular dynamics. This measure protocol has previously been applied to either fluidized or jammed granular systems[36–38] and has been extended to other out of equilibrium systems where inclusions are placed in baths of self-propelled particles.[30–32]

First, in Sec. IV A, we extract the averaged values of the relative and tangential forces between inclusions. Second, in Sec. IV B, we propose a model that captures the long distance behavior of the radial force as a simple function of the shaking amplitude A_0, the relative angle α, and the inclusions' separation distance d. Third, in Sec. IV C, we define the mechanical formation energy of the dimer and compare it to the configurations' probabilities for the freely evolving dimers measured in Sec. III C. Finally, in Sec. IV D, we compute local profile measures of the granular bed along the axis of the dimer to provide further insight into the mechanism underlying the effective interactions between inclusions.

A. Radial and tangential forces

We fix the pair of inclusions at positions $\boldsymbol{X}_a$ and $\boldsymbol{X}_b$, but we let the velocity of the inclusions evolve in time, i.e., we introduce inclusions of infinite mass.[37,38] By allowing the inclusions to acquire a velocity, magnitude present in the grain-inclusion interactions, the disturbance on the granular dynamics introduced by constraining the inclusion displacements is decreased and $F_r(d)$ curves are qualitatively equivalent to the ones obtained by setting to zero the velocity of the inclusions. The forces given by the granular bed on the inclusions are $\boldsymbol{F}_a$ and $\boldsymbol{F}_b$ and define the effective interaction between inclusions. Computing the relative force $\boldsymbol{F}_b(\boldsymbol{X}_b) - \boldsymbol{F}_a(\boldsymbol{X}_a)$, we extract the relevant information of the relative force acting on the dimer. Finally, we project along the radial and transverse directions to extract the averaged contribution of each particle to the effective interactions,

$$F_r(d) = \left\langle \frac{\boldsymbol{F}_b(\boldsymbol{X}_b) - \boldsymbol{F}_a(\boldsymbol{X}_a)}{2} \cdot \hat{\boldsymbol{r}} \right\rangle, \tag{5}$$

$$F_t(d) = \left\langle \frac{\boldsymbol{F}_b(\boldsymbol{X}_b) - \boldsymbol{F}_a(\boldsymbol{X}_a)}{2} \cdot \hat{\boldsymbol{t}} \right\rangle, \tag{6}$$

where unit vectors $\hat{\boldsymbol{r}}$ and $\hat{\boldsymbol{t}}$ define an orthonormal basis of $\mathbb{R}^2$ with $\hat{\boldsymbol{r}} = (\boldsymbol{X}_b - \boldsymbol{X}_a)/|\boldsymbol{X}_b - \boldsymbol{X}_a|$ and, after rotating $\pi/2$, we obtain $\hat{\boldsymbol{t}} = \mathcal{R}_{\pi/2}\hat{\boldsymbol{r}}$. The brackets $\langle\cdot\rangle$ denote the average of the magnitude $(\cdot)$ over cycles and independent realizations of the system.

Inclusions have been placed at configurations with surface to surface distance of the range $d \in [0, 8]$ and angles relative to shaking $\alpha \in [0, \pi/2]$. We average on various sets with fixed parameters α, d, A_0, ϕ to extract the mean values F_r and F_t.

Within this definition of $\hat{\boldsymbol{r}}$ and $\hat{\boldsymbol{t}}$, the projection F_r defines the behavior of the interaction in the radial direction with attractive effective forces captured by negative values of the relative force, $F_r < 0$, and repulsive otherwise. The transverse effective force, F_t, indicates the emergence of a neat torque acting on the dimer with clockwise torques identified by $F_t < 0$ and counterclockwise otherwise. For our dimer configurations in the first quadrant of the plane, clockwise tangential forces align the dimer in the shaking direction.

The relative radial force F_r in Fig. 6 reflects that the effective interaction for a pair of inclusions at contact is attractive. We observe that the magnitude of the force at contact also depends on the orientation of the dimer relative to the shaking direction. The stronger the interaction is, the more aligned—to the shaking—the dimer is. As the distance increases, the force reaches a local maximum before $d = \sigma_g$ and then F_r oscillates with an amplitude that reflects the structure of the grain suspension.

The magnitude and sign of the radial force are sensitive to the orientation of the dimer with respect to the tray shaking direction, α. For perpendicular configurations, the decaying oscillations in the force reflect the structure of the granular bed for long distances as is clear from the persistence of the force oscillations. As the angle is reduced, $\alpha < \pi/2$, the oscillation structure in the radial force is gradually destroyed at long distances, while a neat attractive force remains for several inclusion diameters. Overall, shaking destroys the structure of the granular bed and induces an effective attraction that increases as the dimer aligns relative to the shaking.

In addition to the radial interaction, a torque captured as a relative tangential force F_t appears for configurations with neither $\alpha \neq 0$ nor $\alpha \neq \pi/2$. We have observed a maximum value in the tangential force strength for $\alpha = \pi/4$, which we select to display in Fig. 6. This noncentral force is present in the system for short separation distances, $d \lesssim 2\sigma_g$, and orients the pair along the shaking direction. At $\phi = 0.75$ and $A_0 = 1.5$, a finite dealigning torque clearly emerges at long distances, $d \gtrsim 2\sigma_g$. The nature of the tangential force shown in Fig. 6 is compatible with the anisotropy found in the probability $\mathcal{P}(r_x, r_y)$ for moving inclusions reported in Figs. 2 and 5 in Sec. III.

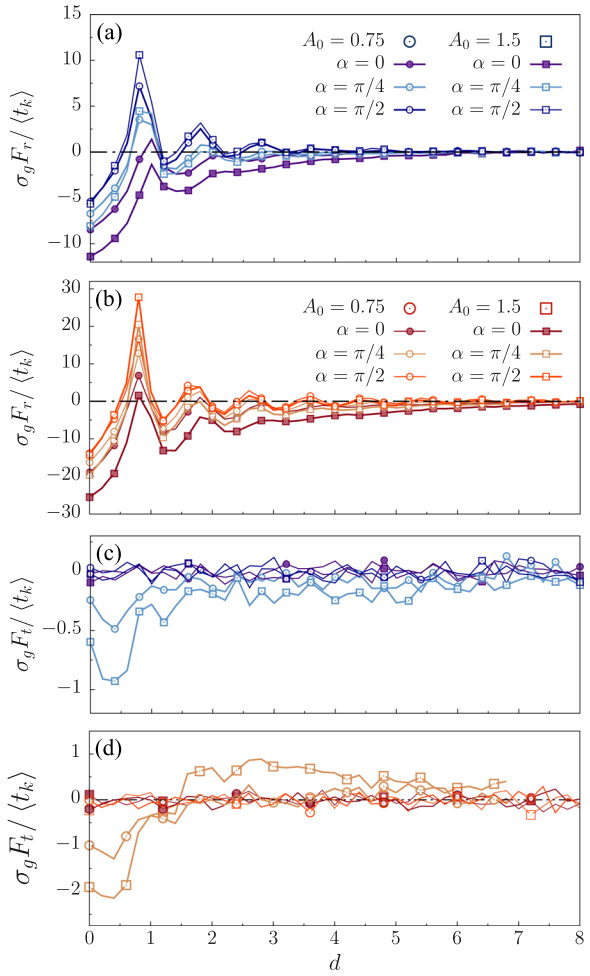

FIG. 6. Effective radial and tangential forces F_r in (a) and (b) and F_t in (c) and (d), respectively. Plots [(a) and (c)] for density $\phi = 0.6$ and [(b) and (d)] for density $\phi = 0.75$. Different amplitudes are labeled by squares, $A_0 = 1.5\sigma_g$, and circles, $A_0 = 0.75\sigma_g$. Different shades of colors identify the dimer angle relative to the shaking direction.

B. Long distance behavior of the radial force

Figure 4 shows that the effective force between inclusions generically displays an attractive, long-range interaction in length scales larger than $10\sigma_g$. Even though we are not able to analyze the functional dependence of this asymptotic decay over several decades, the observed decay is consistent with an algebraic dependence. In granular media, long range forces arising from their nonequilibrium fluctuations have already been described in vibrated systems.[23] For the weak decaying signal of the radial force measure for configurations aligned close to the perpendicular direction, an algebraic fitting curve of the form $F_2(\sigma_g/d)^2$ has proven to be numerically more robust than an exponential decay which is largely interfered by the strong oscillations; see Fig. 7(a). For an algebraic fitting, the strength of the long range interaction is given by the force F_2 and presented in Fig. 7.

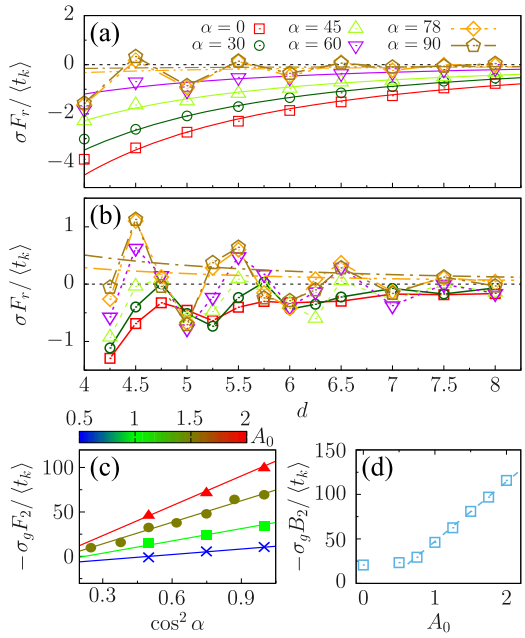

FIG. 7. Long range interaction F_r as a function of interparticle distance, angle, and shaking amplitude. (a) At amplitude $A_0 = 1.5\sigma_g$, the external forcing is strong enough to clearly destroy the internal structure of the gains at $\alpha < 60°$. (b) At $A_0 = 0.5\sigma_g$, the internal structure persists for angles $\alpha \gtrsim 30°$. (c) Strength of the long range force F_2 as a function of $\cos^2 \alpha$ for different shaking amplitudes. (d) Value of the prefactor of $\cos^2 \alpha (\sigma_g/d)^2$ as a function of A_0/σ_g.

To capture the full dependence on α and A_0 on the long range interaction amplitude, F_2, we have systematically swept the space of parameters α and A_0. The structure of the bed of grains is appreciable in both Figs. 7(a) and 7(b); at perpendicular configurations, the emergent long range interaction vanishes, $F_2 \approx 0$. At low values of the shaking amplitude, the grain bed structure persists at lower angles—denoted in dashed lines. As the angle of the dimer decreases, the effect of the external forcing increases and the local granular structure is lost. In this regime, a clear interaction between particles develops and increases as the dimer aligns toward the forcing direction.

To quantify the dependence on the orientation α, we present F_2 as a function of $\cos^2 \alpha$, $F_2 = F_0 \cos^2 \alpha + B_0$, the lowest power of $\cos \alpha$ allowed by the dimer and shaking symmetry, and $B_0 \approx 0$. The results in Fig. 7(c) confirm a quadratic dependence of the cosine on F_2. The analysis of $B_2(A_0)$ in Fig. 7(d) indicates that B_2 essentially remains constant for shaking amplitudes below a value A_0^c followed by a linear increase for $A_0 > A_0^c$.

We combine the previous results to model the effective radial interaction. We report two different behaviors in terms of the shaking amplitude. For shaking amplitudes, $A_0 < A_0^c$, the interaction depends only on the shaking angle and the distance between inclusions as $F_r(\phi) = F_0(\phi)(\sigma_g/r)^2 \cos^2 \alpha$. Second, as the shaking amplitude increases, $A_0 > A_0^c$, the term F_0 acquires an additional term linear on $A_0 - A_0^c$, with slope $F_0\kappa_1$, and can be expressed as

$$F_r(\phi, \boldsymbol{r}) = F_0(\phi)\left[1 + \kappa_1(\phi)\frac{A_0 - A_0^c(\phi)}{\sigma_g}\right]\left(\frac{\sigma_g}{r}\right)^2 \cos^2\alpha,\ A_0 > A_0^c(\phi). \tag{7}$$

Here, we have prescribed an *a priori* dependence on the packing density on each of the parameters. For a system at packing fraction $\phi = 0.75$, we obtain the values of the interaction strength $F_0 = -(21 \pm 1)\langle t_k\rangle/\sigma_g$; $A_0^c = (0.6 \pm 0.1)\sigma_g$, the shaking amplitude above which the interaction increases linearly with increasing A_0; and the dimensionless slope $\kappa_1 = 3.2 \pm 0.3$.

C. Mechanical formation energies

We benefit from Sec. IV B and, in particular, from the radial force displayed in Fig. 6 to define the mechanical formation energy of a dimer aligned at an angle α with respect to the imposed external driving, $\mathcal{U}_\alpha(d)$. Specifically, we define the dimer formation energy as the total mechanical work to bring a pair of inclusions from infinity to a relative distance d along a line at a constant angle,

$$\mathcal{U}_\alpha(d) = \int_{\infty\to d} \boldsymbol{F}_{int}\cdot d\boldsymbol{l} = \int_\infty^d F_r(r,\alpha)dr. \tag{8}$$

In equilibrium, the energy of formation is derived from the probability to measure the pair at a given configuration (d, α) by the simple expression $\mathcal{U} = -k_BT\ln\mathcal{P}$. This relation implies, in particular, that the energy of formation scales with the system temperature, k_BT. Since the granular bed is subject to an energy flux, induced by the tray shaking, we cannot take the previous equality for granted. We subsequently test the validity of this previous relation through an effective bath temperature,[39] $k_BT_{\rm eff}$, that could connect the formation energy to the probability to measure a dimer configuration. To this end, we fit the formation energy of the dimer to the probability to measure the pair of moving inclusions in that dimer configuration. To extract an effective $k_BT_{\rm eff}$ for each set of formation energies $\{\mathcal{U}_\alpha(d_i)\}$ and probabilities $\{\mathcal{P}(d_i,\alpha)\}$ defined at distances $\{d_i\}$, we minimize the chi squared function $\chi^2 = \sum_i\left[\mathcal{U}_\alpha(d_i) - \left(k_BT_{\rm eff}\ln\mathcal{P}(d_i,\alpha) + U_0\right)\right]^2$, with $k_BT_{\rm eff}$ and U_0 as the fitting parameters.

Figure 8 compares the formation energy derived from the relative force and from the angular constrained probabilities with the best fit for $k_BT_{\rm eff}$. The corresponding temperatures depend, in particular, on α, which indicates that it is impossible to describe the dimer behavior as if it was immersed in an effective equilibrium bath; see Table I. Specifically, the obtained formation energies display qualitatively different dependence on the dimer distance when compared to $-k_BT_{\rm eff}\ln P(d)$. For perpendicular configurations, the formation energy of the dimer presents a maximum with $\mathcal{U} > 0$ that decays to zero. The minus logarithm of the probability, instead, presents an absolute minimum and then increases asymptomatically to zero. These qualitative differences do not allow us to describe this system in terms of a $T_{\rm eff}$.

TABLE I. Effective temperature obtained by minimizing χ^2 combining measures of the mechanical formation energy and for the different densities, shaking amplitudes, and orientation angles. Values with missing α correspond to the angular averaged formation energies and probabilities.

A_0	ϕ	α	$k_BT_{\rm eff}$	A_0	ϕ	α	$k_BT_{\rm eff}$
0.75	0.6	0	0.35	0.75	0.75	0	0.24
0.75	0.6	$\pi/4$	0.64	0.75	0.75	$\pi/4$	0.42
0.75	0.6	$\pi/2$	7.4	0.75	0.75	$\pi/2$	1.21
0.75	0.6	...	0.61	0.75	0.75	...	0.46
1.5	0.6	0	0.35	1.5	0.75	0	0.16
1.5	0.6	$\pi/4$	0.46	1.5	0.75	$\pi/4$	0.26
1.5	0.6	$\pi/2$	−0.47	1.5	0.75	$\pi/2$	0.95
1.5	0.6	...	0.39	1.5	0.75	...	0.21

Alternatively, we can extract an effective temperature from the angular averaged probability, $P(d)$; see Fig. 4. To this end, we introduce the angular averaged mechanical formation energy, $\langle\mathcal{U}(d)\rangle_\alpha$, obtained by integrating $\langle F_r\rangle_\alpha \equiv 2/\pi\int_0^{\pi/2} d\alpha\, F_r(d,\alpha)$. Figure 9 shows that the formation energy obtained by the two routes shows semi-quantitative agreement, and also, by construction, we can assign a $T_{\rm eff}$ for each system. Hence, even if the comparison may be misleading, it is possible to interpret the angular average quantities in terms of an effective equilibrium.

Given the distance, and orientation dependence of the radial force, see Eq. (7), the formation energy computed from the angular averaged F_r exhibits a d^{-1} distance dependence. As is shown in

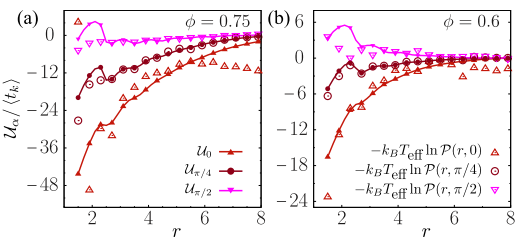

FIG. 8. Mechanical formation energy $\mathcal{U}_\alpha$ in solid lines and the corresponding effective potentials as obtained after minimizing χ^2 for the probability densities $\mathcal{P}(r,\alpha)$ restricted at α. We present shaking amplitudes $A_0 = 0.75\sigma_g$ (a) and $A_0 = 1.5\sigma_g$ (b) at $\phi = 0.75$ with the best fits for the effective temperature $k_BT_{\rm eff}$, as listed in Table I.

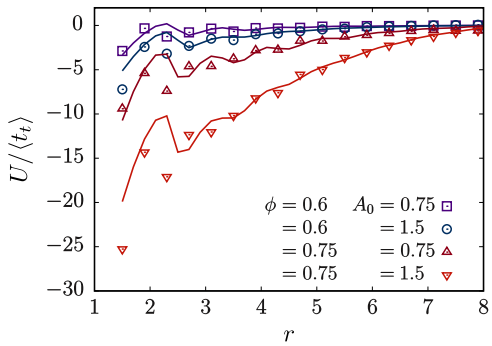

FIG. 9. Angular averaged formation energy $\langle U\rangle_\alpha$ in solid lines compared to the fitted values for $-k_BT_{\rm eff}\ln P(d)$ in points. The values of the corresponding of $k_BT_{\rm eff}$ are given in Table I and labeled by $\alpha-$.

Fig. 4, the same distance decay is found for $-\ln P(d)$, and hence a linear relation between $-\ln P(d)$ and $\langle \mathcal{U} \rangle_\alpha$ is captured at long distances.

D. Kinetic energy excess profiles

We analyze the impact that the inclusions have in the granular bed. Fixing the inclusions allows us not only to measure the relative forces and torques between them but also to quantify the spatial dependence of the physical properties of the grains. We focus on the relative variations of the granular properties along the axis that joins the two dimers. To measure this profile, we consider a rectangular box of size $L \times \sigma_g$ that encloses the inclusions in the axis of the dimer. We subsequently slice this box in cells of width $\Delta x = 0.2\sigma$ and height $\Delta y = 0.2\sigma$ and use them to build the corresponding histograms.

We compute the local density, $\phi(x', y')$, and kinetic energies, $e_k(x', y')$ and $t_k(x', y')$, at each cell with the center at (x', y') and average over oscillation cycles for different initial conditions of the sea of grains. The result is then integrated in the vertical dimension to obtain the dependence on the distance from the surface of an inclusion h. The pair of inclusions define an internal region which is identified as $-d/2 < h < 0$ and an external region $h > 0$. To gain statistics, we combine the results from the profiles centered on each inclusion. For visualization purposes, we plot the negative region from surface to surface $(-d < h < 0)$,

$$\delta e_k(h) = \frac{e_k(h) - \langle e_k \rangle}{\langle e_k \rangle}, \quad \delta t_k(h) = \frac{t_k(h) - \langle t_k \rangle}{\langle t_k \rangle}. \tag{9}$$

In Fig. 10, we display the relative excess of density and kinetic energies for $\phi = 0.75$, $A_0 = 1.5\sigma_g$ relative to the bulk values (9). We compute the profiles for parallel and perpendicular configurations of the dimer and two different separation distances, $d = 2\sigma$ and $d = 6\sigma_g$. For positive values of h, the behavior of each profile does not depend on the dimer separation d. To confirm this dependence, we have computed the profile for a sole inclusion in the system and obtained the same external profiles.

We do not observe a significant deviation of the averaged density along the axis. Moreover, in the region between inclusions, the local density equals to the averaged density outside—except for the density at contact that decays due to the sampling size and the curvature of the disks. However, both kinetic energies—absolute and relative—are not kept constant along h. On the one hand, the excess relative kinetic energy δt_k has a positive value at contact and relaxes to zero. On the other hand, the excess of absolute kinetic energy departs from the negative value and relaxes to zero. For orientations of the dimer perpendicular to the external shaking, δe_k jumps to a positive value and follows the decay of $\delta t_k > 0$ and relaxes to 0, whereas for parallel configurations δe_k does not follow the relative kinetic energy but slowly increases to zero keeping its negative sign.

Finally, we have analyzed the additivity of one-inclusion profiles for the inner region of the dimer, $h < 0$. From the disturbance profile generated by a single particle $\delta p(h)$, as presented in (9), we compute the total disturbance profile in the inner region between independent inclusions located at $h = 0$ and $h = -d$ as $\delta p(-h) + \delta p(d - h)$. We show the additivity of the profiles by comparing the hollow squares and dots to the solid lines in Fig. 10, resulting from the addition of one-inclusion profiles and the computation of the profiles for two-inclusion systems, respectively.

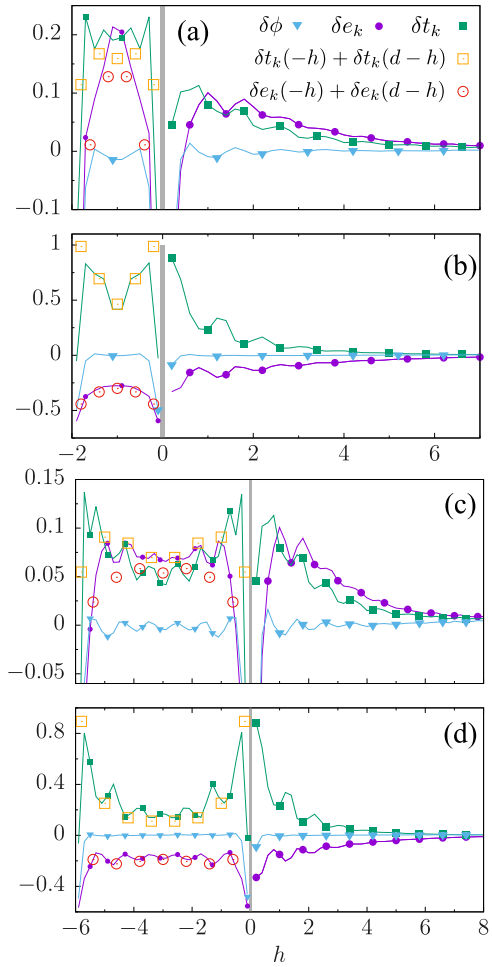

FIG. 10. Excess kinetic energy and density profiles of the granular bed in a system at packing $\phi = 0.75$, forcing amplitude $A_0 = 1.5\sigma_g$, and orientation $\alpha = \pi/2$ in [(a) and (c)] and $\alpha = 0$ in [(b) and (d)]. Positive values of h denote the outer region of the dimer, while negative values of h denote the region between inclusions. Hollow symbols represent the result of the superposition of independent profiles with the origin at $h = 0$ and $h = -d$. In cyan, we plot the relative excess density profile, practically zero, but parallel shaking [(a) and (c)] shows weak oscillations close to the inclusions.

V. CONCLUSIONS

In summary, we have introduced a mechanical model to capture the effective behavior of inclusion in a horizontally shaken granular bed. The analysis of the behavior of an inclusion pair has shown that they have granular mediated noncentral and long range interactions. We have considered a freely moving pair and have computed the forces for a pair at a fixed distance. These two approaches have provided complementary insight.

We have extracted the two dimensional probability density of the relative vector between inclusions and measured a preference of

dimers at contact to align parallel to the external forcing. Consistently, the force measurements with fixed inclusions have revealed the emergence of an attractive force with a maximum for particles at contact plus the emergence of an aligning torque at short distances. The detailed computation of the forces between the two inclusions as a function of the angle they form with the driving force indicates that inclusions tend to remove the ordered structure of the granular bed for $\alpha < \pi/2$ and moderate amplitudes of the shaking $A_0 > \sigma_g/2$. When the granular structure around the inclusions becomes weak in the internal region of the pair, the long range attractive force between the pair becomes apparent. We have characterized the interaction in terms of the parameters of the dimer configuration and shaking of the granular bed with a simple model of interaction at a distance (7). We have matched the anisotropy in the probability $\mathcal{P}(r_x, r_y)$ to the appearance of a neat torque for fixed inclusions. The torque aligns close inclusions $d \lesssim 2\sigma_g$ parallel to the shaking, whereas at $d \gtrsim 4\sigma_g$ and large shaking amplitudes and granular densities, an emergent torque aligns inclusions perpendicularly to the shaking. The appearance of this dealigning torque could be the mechanism leading toward the segregation of mixtures of grains and inclusions into bands perpendicular to the shaking direction.[10,11,24,26] Finally, we have captured the kinetic energy profiles in the granular bed in the immediacies of the inclusion dimer and observed a differentiated behavior of the absolute kinetic energy on the orientation of the dimer. Additionally, we observe that the perturbation of the granular kinetic energies in the internal region of the dimer results from the addition of two independent facing inclusion surfaces.

ACKNOWLEDGMENTS

The authors acknowledge I. Zuriguel for a detailed description of the experimental setup and insightful discussions and Pau Capera for initial simulation results. This work has been supported by MINECO and DURSI under Project Nos. PGC2018-098373-B-100 and 2017 SGR 884, respectively. J.C. was supported by Spanish MECD fellowship FPU13/01911. I.P. also acknowledges SNF Project No. 200021-175719 for funding.

APPENDIX A: STOCHASTIC DYNAMICS OF GRAINS

We present a stochastic integrator for the granular system which the equations of motion (2) presented in Sec. II. In this appendix, we detail the integration of the momenta.

Granular particles are described by the pair of variables position, $\boldsymbol{r}$, and momentum, $\boldsymbol{p}$. With the usual definition of momentum,

$$\frac{d}{dt}\boldsymbol{r}_i(t) = \frac{1}{m_i}\boldsymbol{p}_i(t), \tag{A1}$$

where m_i is the mass of each granular particle and the integral of $\boldsymbol{r}$ is direct. The evolution of the momenta of the particles in the system, $\boldsymbol{p}$, is governed by the following Langevin equation for each particle i:

$$\frac{d}{dt}\boldsymbol{p}_i(t) = \boldsymbol{F}_i(t) - \gamma_{s,i}\left(\frac{\boldsymbol{p}_i(t)}{m_i} - \boldsymbol{v}_s(t)\right) + \boldsymbol{f}_i(t), \tag{A2}$$

where $\gamma_{s,i}$ is the dissipation constant of each grain with the substrate; $\boldsymbol{v}_s(t)$ is the velocity of the substrate; and $\boldsymbol{F}(t)$ and $\boldsymbol{f}(t)$ are the deterministic and random forces, respectively. See Sec. II for the complete description of the model. The random forces, $\boldsymbol{f}$, are modeled as a two dimensional vector with Gaussian components with zero mean and variance $\left\langle f_i^\alpha(t) f_j^\beta(t')\right\rangle = 2\Lambda_\alpha \delta_{\alpha\beta}\delta_{ij}\delta(t-t')$, where Greek indices identify the spatial coordinates and Latin ones label the particles.

To solve Eq. (A2), we separate the terms that depend on the momenta $\boldsymbol{p}$ on the LHS from the deterministic $\boldsymbol{\Phi} = \boldsymbol{F} + \gamma_s \boldsymbol{v}_s$ and random forces $\boldsymbol{f}$ on the RHS,

$$\left(\frac{d}{dt} + \frac{\gamma_{s,i}}{m_i}\right)\boldsymbol{p}_i(t) = \boldsymbol{F}_i(t) + \gamma_{s,i}\boldsymbol{v}_s(t) + \boldsymbol{f}_i(t) = \boldsymbol{\Phi}_i(t) + \boldsymbol{f}_i(t). \tag{A3}$$

The solution to Eq. (A3) is given by the combination $\boldsymbol{p}(t) = \boldsymbol{p}^{(h)}(t) + \boldsymbol{p}^{(p)}(t)$, where $\boldsymbol{p}^{(h)}(t)$ solve the homogeneous equation,

$$\left(\frac{d}{dt} + \frac{\gamma_{s,i}}{m_i}\right)\boldsymbol{p}_i^{(h)}(t) = 0, \tag{A4}$$

after imposing the initial condition on the momenta of the particles $\boldsymbol{p}(t_0)$,

$$\boldsymbol{p}_i^{(h)}(t_0 + \Delta t) = \boldsymbol{p}_i(t_0)\exp\left(-\frac{\gamma_{s,i}}{m_i}\Delta t\right). \tag{A5}$$

$\boldsymbol{p}^{(p)}(t)$ are a particular solution of (A3) and have the form $\boldsymbol{p}^{(p)}(t) = \boldsymbol{\pi}(t)\exp(-\gamma_s/m\, t)$, where $\boldsymbol{\pi}(t)$ satisfy the equation,

$$\frac{d}{dt}\boldsymbol{\pi}_i(t) = \exp\left(\frac{\gamma_{s,i}t}{m_i}\right)\left[\boldsymbol{\Phi}_i(t) + \boldsymbol{f}_i(t)\right]. \tag{A6}$$

Assuming a slow dynamics of the deterministic force $\boldsymbol{\Phi}(t)$ in the interval $[t_0, t_0 + \Delta t]$, the equation is integrated from t_0 to $t_0 + \Delta t$,

$$\boldsymbol{\pi}_i(t_0 + \Delta t) = \boldsymbol{\pi}_i(t_0) + \frac{m_i}{\gamma_{s,i}}\exp\left(\frac{\gamma_{s,i}}{m_i}t_0\right)\left[\exp\left(\frac{\gamma_{s,i}}{m_i}\Delta t\right) - 1\right]\boldsymbol{\Phi}_i(t_0) + \int_{t_0}^{t_0+\Delta t}\exp\left(\frac{\gamma_{s,i}}{m_i}t_1\right)\boldsymbol{f}_i(t_1)\, dt_1\,, \tag{A7}$$

where $\boldsymbol{\Phi}_i(t_0)$ indicates the value of the deterministic computed on particle i with the particles' configurations at time t_0, $\{\boldsymbol{r}(t_0)\}$. We place $\boldsymbol{\pi}(t)$ and $\boldsymbol{p}^{(h)}(t)$ into $\boldsymbol{p}(t)$ to obtain the integral of the momenta after a time Δt,

$$\boldsymbol{p}_i(t_0 + \Delta t) = \boldsymbol{p}_i(t_0)\exp\left(-\frac{\gamma_{s,i}}{m_i}\Delta t\right) + \frac{m_i}{\gamma_{s,i}}\left[1 - \exp\left(-\frac{\gamma_{s,i}}{m_i}\Delta t\right)\right]\boldsymbol{\Phi}_i(t_0) + \int_{t_0}^{t_0+\Delta t}\exp\left[\frac{\gamma_{s,i}}{m_i}(t_1 - t_0 - \Delta t)\right]\boldsymbol{f}_i(t_1)\, dt_1. \tag{A8}$$

Given the statistical invariance of the Gaussian noise, $\boldsymbol{f}(\tau) \equiv \boldsymbol{f}(\tau + t_0)$, we introduce the time shift $\tau = t_1 - t_0$ in the last integral,

$$\boldsymbol{p}_i(t_0 + \Delta t) = \boldsymbol{p}_i(t_0)\exp\left(-\frac{\gamma_{s,i}}{m_i}\Delta t\right) + \frac{m_i}{\gamma_{s,i}}\left[1 - \exp\left(-\frac{\gamma_{s,i}}{m_i}\Delta t\right)\right]\boldsymbol{\Phi}_i(t_0) + \int_0^{\Delta t}\exp\left[\frac{\gamma_{s,i}}{m_i}(\tau - \Delta t)\right]\boldsymbol{f}_i(\tau)\, d\tau. \tag{A9}$$

We have obtained the temporal integration of the particles' momenta up a quadrature. We substitute the last term by a Gaussian random vector, $\boldsymbol{\zeta}_i$, with the same average, $\langle\zeta_i^\alpha\rangle$, and variance, σ_ζ, as the previous integral.

The value of the average is $\langle\zeta_i^\alpha\rangle = 0$ since $\langle f_i^\alpha(t)\rangle = 0$. The variance, however, requires a detailed calculation using the explicit form of the stochastic term in (A9),

$$\begin{aligned}\left(\sigma_{ij}^{\alpha\beta}\right)^2 &= \int_0^{\Delta t} d\tau_1 \int_0^{\Delta t} d\tau_2 \exp\left[\frac{\gamma_{s,i}}{m_i}(\tau_1+\tau_2-2\Delta t)\right]\left\langle \boldsymbol{f}_i(\tau_1)\boldsymbol{f}_j(\tau_2)\right\rangle \\ &= 2\Lambda_\alpha\delta_{ij}\delta_{\alpha\beta}\exp\left(-2\frac{\gamma_{s,i}}{m_i}\Delta t\right)\int_0^{\Delta t} d\tau_1 \exp\left(\frac{\gamma_{s,i}}{m_i}2\tau_1\right) \\ &= \Lambda_\alpha\delta_{ij}\delta_{\alpha\beta}\frac{m_i}{\gamma_{s,i}}\left[1-\exp\left(-2\frac{\gamma_{s,i}}{m_i}\Delta t\right)\right] = 2\sigma_\zeta^2\,\delta_{ij}\delta_{\alpha\beta}. \qquad \text{(A10)}\end{aligned}$$

Finally, we obtain the integration of $\boldsymbol{p}$ as

$$\begin{aligned}\boldsymbol{p}_i(t+\Delta t) &= \exp\left(-\frac{\gamma_{s,i}}{m_i}\Delta t\right)\boldsymbol{p}_i(t) \\ &\quad + \frac{m_i}{\gamma_{s,i}}\left[1-\exp\left(-\frac{\gamma_{s,i}}{m_i}\Delta t\right)\right]\boldsymbol{\Phi}_i(t) + \sigma_\zeta\,\boldsymbol{\zeta}_i, \qquad \text{(A11)}\end{aligned}$$

and $\boldsymbol{\zeta}_i$ is a random vector whose components are random numbers drawn from a Gaussian distribution with zero mean and unit variance. Overall, the evolution of the positions of each particle at each time step is updated with the averaged value of the momentum in times t and $t+\Delta t$,

$$\boldsymbol{r}_i(t+\Delta t) = \boldsymbol{r}_i(t) + \frac{\boldsymbol{p}_i(t)+\boldsymbol{p}_i(t+\Delta t)}{2m_i}\,\Delta t\,. \qquad \text{(A12)}$$

APPENDIX B: GRANULAR MEASURES

In order to characterize the granular bed, we introduce the measure of kinetic energies. For a system under shaking, we can construct either an absolute or a relative kinetic energy,

$$e_k = \frac{1}{N}\sum_i \frac{m_i}{2}|\boldsymbol{v}_i|^2,\ t_k = \frac{1}{N}\sum_i \frac{m_i}{2}|\boldsymbol{v}_i - \boldsymbol{V}_{cm}|^2, \qquad \text{(B1)}$$

with $\boldsymbol{V}_{cm}$ as the center of mass velocity. The usual magnitude[39] defined in granular systems is t_k, but the introduction of external bodies gives a certain relevance to e_k. Here, we discuss the advantages of using each of them to scale the interaction forces obtained in Sec. IV.

The relative kinetic energy t_k does not depend on the shaking amplitude A_0, and it is best suited to compare forces in systems at different shaking amplitudes and granular properties such as the mean squared displacement.

The absolute kinetic energy e_k includes the flux of energy that the shaking introduces to the grains, and it is relevant for the interactions with external bodies. Even though both energies are suitable to define an energy scale, we choose the averaged t_k for the sake of commensurability.

In Fig. 11, we present the dependence of the averaged energies measured at different densities, forcing amplitudes, and Λ_x, for a system with fixed granular parameters, $\Lambda_x/\Lambda_y = 2$, $k = 2.5\cdot 10^4$, $\gamma_s = 20$, and $\gamma = 33$ in system units.

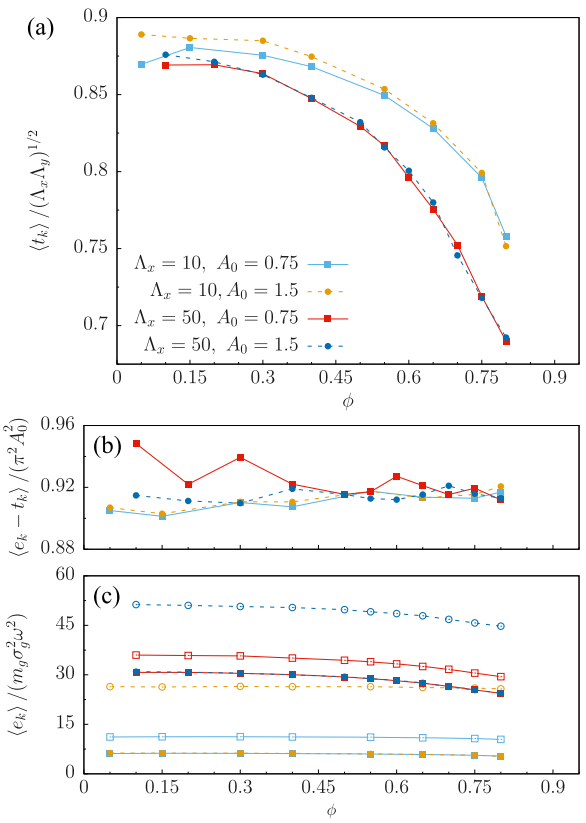

FIG. 11. Measures of kinetic energies as for increasing the packing density of grains. In solid lines, we plot the measures. (a) The relative kinetic energy normalized by the random force. (b) The difference in kinetic energies expected to be $\langle e_k - t_k\rangle \approx \pi^2 A_0^2$. (c) The absolute kinetic energy of the grains compared to the acceleration unit given by $m_g\sigma_g^2\omega^2$.

We observe a decay of the kinetic energy as the density of grains increases. Dissipation in particle-particle collision events in granular systems introduces an energy loss, and it is responsible for the energy dissipation of grains as density increases. The difference in kinetic energies is solely due to the external shaking, and it is confirmed in Fig. 11(b) where the kinetic energy difference remains approximately constant in the considered packing fraction range. We determine a monolayer to be dense when the energy loss is relevant, in this case for $\phi > 0.6$. Since we are interested in a dense system, we determine our lower bound for the packing range to be $\phi = 0.6$.

The upper bound for the packing fraction must correspond to a system within the same mobility regime. For this purpose, we measure the jump distribution of grains, $P(\Delta)$, as the probability density distribution of the displacement, Δ, of grains after a time unit.

Figure 12 shows a Gaussian jump distributions for $\phi \le 0.75$ at $\Lambda_x = 50$. For this reason, we set the packing upper limit for exploration in this paper at $\phi = 0.75$.

At larger densities, for example, $\phi = 0.8$, the jump distribution presents a pronounced peak at $|\Delta| \approx 0$ that indicates the caging effect

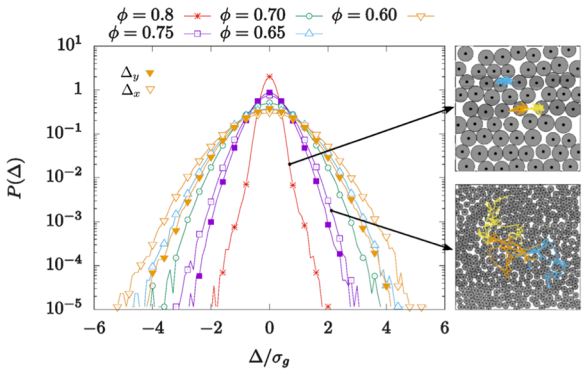

FIG. 12. Displacement statistics of granular particles between shaking cycles. Plots of the system with three representative trajectories.

of the neighboring grains and it is no longer Gaussian. Mean squared displacements, not shown here, also confirm the caging of grains, and thus, the system is not in a dense fluidized regime.

REFERENCES

[1]H. M. Jaeger, S. R. Nagel, and R. P. Behringer, Rev. Mod. Phys. **68**, 1259 (1996).
[2]A. J. Liu and S. R. Nagel, Nature **396**, 21 (1998).
[3]M. E. Cates, J. P. Wittmer, J.-P. Bouchaud, and P. Claudin, Phys. Rev. Lett. **81**, 1841 (1998).
[4]J. M. Ottino and D. V. Khakhar, Annu. Rev. Fluid Mech. **32**, 55 (2000).
[5]A. Kudrolli, Rep. Prog. Phys. **67**, 209 (2004).
[6]I. S. Aranson and L. S. Tsimring, Rev. Mod. Phys. **78**, 641 (2006).
[7]S. Godoy, D. Risso, R. Soto, and P. Cordero, Phys. Rev. E **78**, 031301 (2008).
[8]M. P. Ciamarra, M. D. D. Vizia, A. Fierro, M. Tarzia, A. Coniglio, and M. Nicodemi, Phys. Rev. Lett. **96**, 058001 (2006).
[9]D. A. Sanders, M. R. Swift, R. M. Bowley, and P. J. King, Phys. Rev. Lett. **93**, 208002 (2004).
[10]T. Mullin, Phys. Rev. Lett. **84**, 4741 (2000).
[11]P. M. Reis and T. Mullin, Phys. Rev. Lett. **89**, 244301 (2002).
[12]P. M. Reis, T. Sykes, and T. Mullin, Phys. Rev. E **74**, 051306 (2006).
[13]M. Pica Ciamarra, A. Coniglio, and M. Nicodemi, Eur. Phys. J. E **22**, 227 (2007).
[14]S. Aumaître, C. A. Kruelle, and I. Rehberg, Phys. Rev. E **64**, 041305 (2001).
[15]E. Opsomer, N. Vandewalle, M. Noirhomme, and F. Ludewig, Eur. Phys. J. E **37**, 115 (2014).
[16]T. Masuda, K. Nishinari, and A. Schadschneider, Phys. Rev. Lett. **112**, 138701 (2014).
[17]C. Lozano, A. Janda, A. Garcimartín, D. Maza, and I. Zuriguel, Phys. Rev. E **86**, 031306 (2012).
[18]I. Zuriguel, D. R. Parisi, R. C. Hidalgo, C. Lozano, A. Janda, P. A. Gago, J. P. Peralta, L. M. Ferrer, L. A. Pugnaloni, E. Clément *et al.*, Sci. Rep. **4**, 7324 (2014).
[19]C. Salueña, T. Pöschel, and S. E. Esipov, Phys. Rev. E **59**, 4422 (1999).
[20]T. Pöschel, T. Schwager, and C. Salueña, Phys. Rev. E **62**, 1361 (2000).
[21]G. H. Ristow, G. Straßburger, and I. Rehberg, Phys. Rev. Lett. **79**, 833 (1997).
[22]M. Kardar and R. Golestanian, Rev. Mod. Phys. **71**, 1233 (1999).
[23]C. Cattuto, R. Brito, U. M. B. Marconi, F. Nori, and R. Soto, Phys. Rev. Lett. **96**, 178001 (2006).
[24]M. P. Ciamarra, A. Coniglio, and M. Nicodemi, Phys. Rev. Lett. **97**, 038001 (2006).
[25]C. Lozano, I. Zuriguel, A. Garcimartín, and T. Mullin, Phys. Rev. Lett. **114**, 178002 (2015).
[26]P. M. Reis, G. Ehrhardt, A. Stephenson, and T. Mullin, Europhys. Lett. **66**, 357 (2004).
[27]R. C. Hidalgo, I. Zuriguel, D. Maza, and I. Pagonabarraga, Phys. Rev. Lett. **103**, 118001 (2009).
[28]T. Pöschel and T. Schwager, *Computational Granular Dynamics: Models and Algorithms* (Springer Science & Business Media, 2005).
[29]M. P. Allen and D. J. Tildesley, *Computer Simulation of Liquids* (Oxford University Press, 1989).
[30]J. Harder, S. Mallory, C. Tung, C. Valeriani, and A. Cacciuto, J. Chem. Phys. **141**, 194901 (2014).
[31]R. Ni, M. A. Cohen Stuart, and P. G. Bolhuis, Phys. Rev. Lett. **114**, 018302 (2015).
[32]M. Zaeifi Yamchi and A. Naji, J. Chem. Phys. **147**, 194901 (2017).
[33]G. M. Torrie and J. P. Valleau, J. Comput. Phys. **23**, 187 (1977).
[34]D. Frenkel and B. Smit, *Understanding Molecular Simulation: From Algorithms to Applications* (Elsevier, 2001), Vol. 1.
[35]J. Kästner, Wiley Interdiscip. Rev. Comput. Mol. Sci. **1**, 932 (2011).
[36]M. R. Shaebani, J. Sarabadani, and D. E. Wolf, Phys. Rev. Lett. **108**, 198001 (2012).
[37]M. R. Shaebani, J. Sarabadani, and D. E. Wolf, Phys. Rev. E **88**, 022202 (2013).
[38]J.-J. Liétor-Santos and J. C. Burton, Soft Matter **13**, 1142 (2017).
[39]C. Song, P. Wang, and H. A. Makse, Proc. Nat. Acad. Sci. U. S. A. **102**, 2299 (2005).